DELFT UNIVERSITY OF TECHNOLOGY

REPORT 10-23

Numerical Methods For Industrial Problems With Phase Changes

Ibrahim, F. J. Vermolen, C. Vuik

1. INTRODUCTION

Physical models for multi-phase fluid systems in porous media have applications in industrial processes such as drying, steam production, oil recovery, and freezing. One of the primary objectives of these models is to simulate the process to enhance the quality of the product and improve the process itself in terms of efficiency, cost etc. Food items, in general, can be considered as a porous medium (bread, potato etc). In the context of the numerical density-enthalpy method (henceforth called ρ-h method), Arendsen has presented many applications in his work [1, 3, 4] (a boiler system, potato drying etc). Since several types of phases are present, the interface between adjacent phases has to be tracked. The so called moving interface problems or free boundary problems, are typically solved by methods such as the level-set, moving-grid, and the phase-field model [8–10]. Level-set and moving-grid models use a sharp interface between adjacent phases. In contrast, the phase-field model allows a diffuse region where, for example, the mass density between the two coexisting phases varies smoothly from one phase to the other [9]. On the other hand, the numerical ρ-h method uses only one set of equations and it does not require an explicit tracking of phase change boundaries. These two merits make this method potentially faster and relatively stable. In [1, 3] a comparison is made between the ρ-h method and standard approaches for modeling thermal processes with a phase change. It is common practice to solve the energy or mass balance equations alone or to assume constant boiling pressure and temperature. Arendsen also explained that only taking the energy or mass balance is valid for a limited range and that their physical basis is incomplete. Furthermore, the assumption of a constant ambient pressure and a fixed phase-change temperature profile cannot always be justified [1, 6]. The $1D$ and $2D$ models are presented and solved in [2, 6, 16]. However, the IMEX time integration method used in these paper to solve the nonlinear problem does not lead to a practically useful time step Δt. Furthermore a fully implicit time integration, with a certain choice of Picard Iteration to solve the nonlinear problem also led to an unfeasibly small time step Δt. Presently, we consider a fully-implicit time integration combined with Newton-Raphson linearization. For our test problems, where the initial value of X_G (the gas mass fraction) is continuous, we do not have any condition on Δt for stability. The problem can be solved in one time-step for our desired level of accuracy. Standard Galerkin finite elements are considered for the spatial discretization.

The report is divided into five sections with the following outline. In the first section, the (ρ, h)-model is introduced and briefly compared with other methods, which deal with phase changing flow problems. In the second section, the mathematical model of the problem is provided that we solve and discuss in this report. The section also contains a discussion on the solution strategy that we use and the previously used time-integration methods such as the IMEX method and Picard iteration. Furthermore, we have shown under which conditions the problem is well-posed with respect to the boundary conditions. In the third section, we present the numerical solution algorithm in detail. The standard Galerkin algorithm, Euler Backward, and Newton-Raphson time integration methods are the main ingredients of the solution strategy. Simulation results are provided in Section four, whereas the last section contains the important conclusions and future work.

2. The problem definition

We start this section with the $2D$ mathematical model. It consists of mass and energy conservation laws, Darcy's law, and other thermodynamical relations. The $1D$ model is analogous to it and given in [2,16].

2.1. **The mathematical model.** We consider the flow of propane (C_3H_8) in a unit square (porous medium) where the interior is represented by Ω and the boundary is designated by Γ. The mathematical model for the two-dimensional system is given by the following equations.

$$\frac{\partial \rho}{\partial t} + \boldsymbol{\nabla} \cdot (\rho \boldsymbol{v}) = 0, \qquad \boldsymbol{x} \in \Omega, \ t > 0, \ \text{(mass conservation)}, \tag{1}$$

$$\frac{\partial s}{\partial t} + \boldsymbol{\nabla} \cdot (s\boldsymbol{v}) - \boldsymbol{\nabla} \cdot (\lambda \boldsymbol{\nabla} T) = q, \qquad \boldsymbol{x} \in \Omega, \ t > 0, \ \text{(energy conservation)}, \tag{2}$$

$$\boldsymbol{v} + \frac{K}{\mu} \boldsymbol{\nabla} P = 0, \qquad \boldsymbol{x} \in \Omega, \ t > 0, \ \text{(Darcy's law)}. \tag{3}$$

$$T = T(\rho, h), \qquad \boldsymbol{x} \in \Omega, \ t > 0, \ \text{(thermodynamical relation)}, \tag{4}$$

$$P = P(\rho, h), \qquad \boldsymbol{x} \in \Omega, \ t > 0, \ \text{(thermodynamical relation)}, \tag{5}$$

$$s = \rho h, \qquad \boldsymbol{x} \in \Omega, \ t > 0, \ \text{(total enthalpy)}, \tag{6}$$

$$X_G = X_G(\rho, h), \qquad \boldsymbol{x} \in \Omega, \ t > 0, \ \text{(thermodynamical relation)}, \tag{7}$$

where the permeability K, dynamic viscosity μ, and heat diffusivity λ are assumed to be constants and q is a heat source. The velocity $\boldsymbol{v}$ consists of two components v_x and v_y (i.e., $\boldsymbol{v} =< v_x, v_y >$) whereas $\boldsymbol{\nabla} =< \frac{\partial}{\partial x}, \frac{\partial}{\partial y} >$. We neglected gravitational effects because gravity does not play a role in our test cases. The density (ρ) and enthalpy (h) are taken as state variables. Other variables such as temperature (T), pressure (P), and gas mass fraction (X_G) are computed by using ρ-h diagrams as explained in the next subsection. The computation of X_G is a postprocessing step. From a practical point of view, it is more convenient to set initial values in terms of T and X_G. Initial values for other solution variables can be computed from them through phase diagrams. In [2], we used Robin boundary conditions but here we restrict our numerical experiments to an adiabatic and mass isolated system. The initial and boundary conditions are given as follows

$$T(\boldsymbol{x}, 0) = T_0(\boldsymbol{x}) \qquad \boldsymbol{x} \in \Omega,$$

$$X_G(\boldsymbol{x}, 0) = X_{G,0}(\boldsymbol{x}) \qquad \boldsymbol{x} \in \Omega,$$

$$\rho \boldsymbol{v} \cdot \boldsymbol{n} = 0 \qquad \boldsymbol{x} \in \Gamma, \ t > 0 \qquad \text{(zero mass flux)}, \tag{8}$$

$$-\lambda \frac{\partial T}{\partial \boldsymbol{n}} + s\boldsymbol{v} \cdot \boldsymbol{n} = 0 \qquad \boldsymbol{x} \in \Gamma, \ t > 0 \qquad \text{(zero energy flux)}, \tag{9}$$

where $\boldsymbol{n}$ is a unit normal to the boundary. Further remarks on density-enthalpy diagrams, linearization schemes, and the use of Robin boundary conditions for this model are made in the following subsections.

2.2. **Density-enthalpy phase diagrams.** In this report we use the mass and energy balances together and use density ρ and enthalpy h as our state variables. These coupled partial differential equations together with other relations are solved by using finite elements (the standard Galerkin algorithm). A set of ρ-h diagrams is used to determine temperature T, pressure P, and mass fractions [1]. In Figure 1, three such diagrams are shown for Propane (C_3H_8). Each curve is obtained
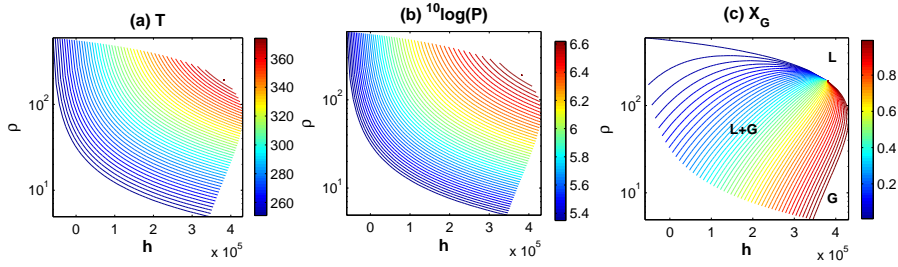
FIGURE 1. ρ-h diagrams for C_3H_8, (a) Plots of isotherms, (b) isobars, and (c) constant gas mass fraction curves.

through constrained minimization of the total Gibbs free energy as a function of T, P, and mass distribution at given ρ and h [1]. For a given substance (e.g., C_3H_8) we have a unique set of ρ-h diagrams. These diagrams work in a similar way as lookup tables (in the solution algorithm), where ρ and h act as row and column, respectively, whereas the curve color serves as the table entry for the corresponding variable (i.e., P, T, or X_G). In Figure 1(c), liquid and gas phases are labeled as 'L' and 'G' respectively. The transitional zone is marked with '$L + G$' which is noticeably larger than the 'L' and 'G' zones. Other sets of phase diagrams are also available, which provide, for example, a transformation from (T, X_G) to $(\rho, h,$ and $P)$. These transformations are also used when initial conditions are specified in T and X_G.

2.3. **The solution strategy.** The $2D$ model is numerically solved over a unit square (and $1D$ model is solved over a unit line segment) with uniform spatial steps. The standard Galerkin algorithm is used for the spatial discretization. The Newton-Raphson method is used to linearize the system as follows. Let the nonlinearly coupled system of equations be arranged in the homogeneous form

$$\boldsymbol{f}(\boldsymbol{x}) = \boldsymbol{0},$$

where $\boldsymbol{f}$ and $\boldsymbol{x}$ are vectors of the same dimension. The vector $\boldsymbol{x}$ is the required solution set and $\boldsymbol{f}$ represents a set of relations between them including nonlinear partial differential equations. The Taylor expansion of $\boldsymbol{f}(\boldsymbol{x})$ about $\boldsymbol{x}^k$ (for some k) is expressed as

$$\boldsymbol{f}(\boldsymbol{x}^k) + \left.\frac{\partial \boldsymbol{f}}{\partial \boldsymbol{x}}\right|_{\boldsymbol{x}=\boldsymbol{x}^k} \boldsymbol{\delta x} + \frac{1}{2}\, \boldsymbol{\delta x}^T \left.\frac{\partial^2 \boldsymbol{f}}{\partial \boldsymbol{x}^2}\right|_{\boldsymbol{x}=\boldsymbol{x}^k} \boldsymbol{\delta x} + ... = \boldsymbol{0},$$

where $\boldsymbol{\delta x} = \boldsymbol{x}^{k+1} - \boldsymbol{x}^k$, $J = \left.\frac{\partial \boldsymbol{f}}{\partial \boldsymbol{x}}\right|_{\boldsymbol{x}=\boldsymbol{x}^k}$ is the Jacobian matrix, and $\left.\frac{\partial^2 \boldsymbol{f}}{\partial \boldsymbol{x}^2}\right|_{\boldsymbol{x}=\boldsymbol{x}^k}$ is the Hessian matrix. Assuming that $\boldsymbol{f}(\boldsymbol{x})$ is sufficiently smooth in the neighborhood of $\boldsymbol{x}^k$, we approximate $\boldsymbol{f}(\boldsymbol{x})$ by first two terms of its Taylor's expansion. This leads to

$$\boldsymbol{f}(\boldsymbol{x}^k) + J\,(\boldsymbol{x}^{k+1} - \boldsymbol{x}^k) = \boldsymbol{0},$$

or

$$\boldsymbol{x}^{k+1} = \boldsymbol{x}^k - J^{-1} \boldsymbol{f}(\boldsymbol{x}^k).$$

Hence, the linearization actually leads to a Newton-Raphson iteration making k as index of the Newton loop. For a programming point of view we execute the Newton loop for each time iteration τ. Depending on the running error ϵ_r and the error tolerance ϵ_{min}, we examine whether convergence has been reached or whether the loop should be continued or stopped if the solution diverges.

2.4. **Time integration schemes.** For the given system of nonlinear equations, we applied a number of linearization schemes such as the IMEX [16] method, the Picard iteration [2] (for fully implicit time itegration), and presently we use a Newton-Raphson iteration. Furthermore we proposed Robin boundary conditions in [2, 16]. A short description of these issues is as follows.

2.4.1. *IMplicit-EXplicit (IMEX) method.* Let u^τ denote the approximation of the variable $u(\boldsymbol{x}, t)$ at $t = \tau \, \Delta t$. In this case the mass and energy equations are integrated in time in the following manner.

$$\frac{1}{\Delta t}(\rho^\tau - \rho^{\tau-1}) + \boldsymbol{\nabla} \cdot (\rho^\tau \boldsymbol{v}^{\tau-1}) = 0 \quad \text{(mass equation)} , \quad (10)$$

$$\frac{1}{\Delta t}(s^\tau - s^{\tau-1}) + \boldsymbol{\nabla} \cdot (s^\tau \boldsymbol{v}^{\tau-1}) - \lambda \boldsymbol{\nabla} \cdot \boldsymbol{\nabla} T^{\tau-1} = 0 \quad \text{(energy equation)} . \quad (11)$$

With this linearization scheme, these equations are quasi-hyperbolic PDEs in the sense that the second order spatial derivatives only mimic a source term. Hence, the boundary conditions apply only when the mass flows into the system, i.e., when $\boldsymbol{v} \cdot \boldsymbol{n} < 0$, where $\boldsymbol{n}$ is the unit normal at the boundary. Boundary conditions as provided in [16] are the following

$$\rho^\tau \boldsymbol{v}^{\tau-1} \cdot \boldsymbol{n} = \begin{cases} k_m(\rho^{\tau-1} - \rho_a), & \text{if } \boldsymbol{v}^{\tau-1} \cdot \boldsymbol{n} < 0, \\ \rho^\tau \boldsymbol{v}^{\tau-1} \cdot \boldsymbol{n}, & \text{if } \boldsymbol{v}^{\tau-1} \cdot \boldsymbol{n} > 0, \end{cases}$$

$$-\lambda \frac{\partial T^{\tau-1}}{\partial \boldsymbol{n}} + s^\tau \boldsymbol{v}^{\tau-1} \cdot \boldsymbol{n} = \begin{cases} k_h(T^{\tau-1} - T_a) + h_a \, k_m(\rho^{\tau-1} - \rho_a), & \text{if } \boldsymbol{v}^{\tau-1} \cdot \boldsymbol{n} < 0, \\ k_h(T^{\tau-1} - T_a) + s^\tau \boldsymbol{v}^{\tau-1} \cdot \boldsymbol{n}, & \text{if } \boldsymbol{v}^{\tau-1} \cdot \boldsymbol{n} > 0. \end{cases}$$

Since the diffusion term is treated explicitly therefore the time step Δt is bounded by some δ_b i.e.,

$$\Delta t \leq \delta_b.$$

For a linear diffusion PDE

$$\frac{\partial \rho}{\partial t} - \lambda \boldsymbol{\nabla} \cdot \boldsymbol{\nabla} \rho = 0,$$

a necessary condition for the solution convergence is

$$\delta_b = \frac{(\Delta x)^2 \, (\Delta y)^2}{2\lambda((\Delta x)^2 + (\Delta y)^2)},$$

on a rectangular mesh with finite differences, where Δx and Δy are spatial step sizes in respective directions. A similar relation can be derived for finite-element discretization. The upper bound for Δt as determined for a convection-diffusion equation serves as an estimate for the kind of solution scheme we consider in [16]. This relation shows that a high resolution mesh would result in a small time step which leads to an excessive computation. In order to overcome this difficulty with the choice of Δt, we tried the following time integration scheme.

2.4.2. *Picard iteration.* In [2], the time integration of the energy equation is given by

$$\frac{1}{\Delta t}(s^{\tau,p} - s^{\tau-1}) + \boldsymbol{\nabla} \cdot (s^{\tau,p} \boldsymbol{v}^{\tau,p-1}) - \lambda \boldsymbol{\nabla} \cdot \boldsymbol{\nabla} T^{\tau,p-1} = 0,$$

where τ is the current value of the time loop index and p is the Picard loop index. Note that the diffusion term is taken at the previous Picard iteration. For the weak formulation and standard Galerkin algorithm for this equation, see [2]. At the start of a Picard iteration, an initial guess for the solution variables is required. In [2], the initial guess is the solution variables at $\tau - 1$ (e.g., $T^{\tau,p-1}$ is assigned $T^{\tau-1}$).

Therefore the energy equation has actually the following form at the start of each Picard loop, when $p = 1$

$$\frac{1}{\Delta t}(s^{\tau,1} - s^{\tau-1}) + \boldsymbol{\nabla} \cdot (s^{\tau,1} \, \boldsymbol{v}^{\tau-1}) - \lambda \boldsymbol{\nabla} \cdot \boldsymbol{\nabla} T^{\tau-1} = 0.$$

Again, the diffusion term is explicit in τ and therefore the upper bound for Δt as discussed in IMEX case applies here as well. Hence, the Picard iteration in this case does not offer any advantage over IMEX with respect to choosing a larger Δt. In this report, the Newton-Raphson method is applied for the system linearization as discussed in Subsection 2.3. However, first we show that certain thermodynamical relations among the solution variables, with nonhomogeneous Robin boundary conditions, make the problem ill-posed.

2.5. **The use of Robin boundary conditions in the ρ-h model.** In [2], we proposed the following boundary conditions

$$\rho \boldsymbol{v} \cdot \boldsymbol{n} = k_m(\rho - \rho_a), \qquad \text{(for mass equation)} , \qquad (12)$$

$$-\lambda \frac{\partial T}{\partial \boldsymbol{n}} + s\boldsymbol{v} \cdot \boldsymbol{n} = k_h(T - T_a) + h_\Gamma k_m(\rho - \rho_a), \qquad \text{(for energy equation)} . \qquad (13)$$

where k_m and k_h are transfer coefficients for the transport of mass and heat. Other parameters are the ambient density ρ_a, ambient temperature T_a, and enthalpy at the boundary h_Γ. We no longer restrict the boundary conditions to inflow only because the mass and energy equations do not have a quasi-hyperbolic structure in the continuous problem. Hence, it is necessary to use boundary conditions on each point of the boundary. To make this point clear, consider the mass equation.

$$\frac{\partial \rho}{\partial t} + \boldsymbol{\nabla} \cdot (\rho \boldsymbol{v}) = 0.$$

Using $v = -\frac{K}{\mu} \boldsymbol{\nabla} P$ in this equation. We get

$$\frac{\partial \rho}{\partial t} - \frac{K}{\mu} \boldsymbol{\nabla} \cdot (\rho \, \boldsymbol{\nabla} P) = 0. \qquad (14)$$

Using the differential of $P(\rho, h)$

$$\boldsymbol{\nabla} P = \frac{\partial P}{\partial \rho} \boldsymbol{\nabla} \rho + \frac{\partial P}{\partial h} \boldsymbol{\nabla} h,$$

into equation (14). This yields

$$\frac{\partial \rho}{\partial t} - \frac{K}{\mu} \boldsymbol{\nabla} \cdot \left[\rho \left(\frac{\partial P}{\partial \rho} \boldsymbol{\nabla} \rho + \frac{\partial P}{\partial h} \boldsymbol{\nabla} h \right) \right] = 0.$$

Hence we have shown that the mass equation indirectly contains a diffusion term in ρ and therefore it can not be considered as a hyperbolic partial differential equation. The same holds for a purely implicit time integration. An analogous derivation can be carried out for the energy equation.

The use of these boundary conditions on our specific thermodynamic system leads to solutions near boundaries (abrupt changes or steep gradients) which could not entirely be justified. To prove that these boundary conditions are ill-conditioned for our specific thermodynamic system, we proceed with the following arguments. In the ρ-h model, the pair (T, X_G) is sufficient to determine the rest of the system variables like ρ, h, P, v, etc. The total differential of $P(T, X_G)$, in this case, is defined as

$$\boldsymbol{\nabla} P = \frac{\partial P}{\partial T} \boldsymbol{\nabla} T + \frac{\partial P}{\partial X_G} \boldsymbol{\nabla} X_G, \qquad (15)$$

Now we found that certain substances exhibit the property $\frac{\partial P}{\partial X_G} = 0$. In [2] the substance under discussion is Propane (C_3H_8). In Figure 2(a), the relation between P and T is shown for $0 < X_G < 1$, which is a unique curve. Figure 2(b) shows plots
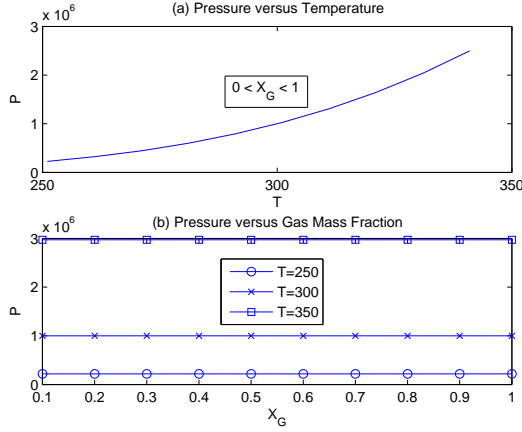
FIGURE 2. . Pressure relation with temperature and gas mass fraction.

of P against X_G for three temperature values. Clearly $\frac{\partial P}{\partial X_G} = 0$ for $250 \leq T \leq 350$. Therefore, equation (15) reduces to

$$\boldsymbol{\nabla} P = \frac{\partial P}{\partial T} \boldsymbol{\nabla} T, \tag{16}$$

where $\frac{\partial P}{\partial T}$ is nonzero (refer to Figure 2(a)).

Next, we multiply equation (12) by h_Γ and subtract it from equation (13), then we obtain

$$-\lambda \boldsymbol{\nabla} T \cdot \boldsymbol{n} = k_h (T - T_a), \quad \text{(at boundary, } s = \rho h_\Gamma),$$

$$-\lambda \frac{1}{\left(\frac{\partial P}{\partial T}\right)} \boldsymbol{\nabla} P \cdot \boldsymbol{n} = k_h (T - T_a), \quad \text{(follows from eq. (16)),}$$

$$\frac{\lambda \mu}{K} \frac{1}{\left(\frac{\partial P}{\partial T}\right)} \boldsymbol{v} \cdot \boldsymbol{n} = k_h (T - T_a), \quad \text{(follows from Darcy's Law).}$$

Combination with equation (12), gives

$$k_h = k_m \frac{\lambda \mu}{k \frac{\partial P}{\partial T}} \frac{(\rho - \rho_a)}{\rho (T - T_a)},$$

which shows that k_m and k_h in this case cannot be chosen independently. Furthermore the relation is time-dependent and nonlinear except for $k_m = k_h = 0$. Therefore the proposed Robin boundary conditions are ill-conditioned if $\frac{\partial P}{\partial X_G} = 0$. Hence, for this case, we proved the following porposition.

Proposition 1. *If $\frac{\partial P}{\partial X_G} = 0$, then the problem stated by equations (1-7) supplied with initial conditions and boundary conditions as in equations (12) and (13) is ill-posed if either k_h or k_m (or both) is nonzero.*

Presently, we consider an isolated system, i.e., $k_m = k_h = 0$, so the problem is well-posed.

2.6. **Simulation results validation.** As far as we know, the analytical solution of the system of PDEs that we solve in this report is unknown. We solve the system numerically over Ω and validate the results on the basis of physical laws such as Fourier's Law of thermal conduction and mass and energy conservation etc. The steady-state values of T, P, and v are used to compare the results as obtained by solving the nonlinear problem. Furthermore, we have compared solution variables by using $1D$ and $2D$ models by setting similar $1D$ conditions.

We also observe the system response to an initial step function in the gas mass

fraction X_G, i.e., we set a sharp interface between two different gas-liquid compositions. This helps to determine the robustness of the numerical method and to link the present model to sharp interface models.

3. METHOD DESCRIPTION

To solve the fluid system with finite elements (with quadrilateral elements and bilinear basis functions), we start with the Euler backward time discretization of the partial differential equations followed by obtaining the weak formulations, Newton-Raphson linearization and finally a spatial discretization by using standard Galerkin algorithm. The weak formulation also incorporates the homogeneous boundary conditions as given by equations (8) and (9).

3.1. **Numerical treatment of the mass equation.** In order to get the weak formulation, we discretize equation (1) in time using the Euler backward scheme, multiply it by a test function $\phi(\boldsymbol{x})$, and integrate over Ω

$$\frac{1}{\Delta t} \int_{\Omega} (\rho^{\tau} - \rho^{\tau-1})\phi(\boldsymbol{x})d\boldsymbol{x} + \int_{\Omega} \boldsymbol{\nabla} \cdot (\rho^{\tau} \boldsymbol{v}^{\tau})\phi(\boldsymbol{x}) \ d\boldsymbol{x} = 0, \ 1 \le \tau \le \tau_{max}, \qquad (17)$$

where τ is a time index. In order to determine the solution at a defined time, the number of time iterations τ_{max} depends on the value of the time step (Δt) between successive iterations. Now using the vector product rule

$$\boldsymbol{\nabla} \cdot (\rho \boldsymbol{v} \phi) = \phi \boldsymbol{\nabla} \cdot (\rho \boldsymbol{v}) + \rho \boldsymbol{v} \cdot \boldsymbol{\nabla} \phi,$$

and the divergence theorem

$$\int_{\Omega} \boldsymbol{\nabla} \cdot \boldsymbol{F} d\boldsymbol{x} = \int_{\Gamma} \boldsymbol{F} \cdot \boldsymbol{n} d\Gamma,$$

in equation (17) we have

$$\frac{1}{\Delta t} \int_{\Omega} (\rho^{\tau} - \rho^{\tau-1})\phi d\boldsymbol{x} + \int_{\Gamma} \rho^{\tau} \boldsymbol{v}^{\tau} \phi \cdot \boldsymbol{n} d\Gamma - \int_{\Omega} \rho^{\tau} \boldsymbol{v}^{\tau} \cdot \boldsymbol{\nabla} \phi d\boldsymbol{x} = 0.$$

We apply the boundary condition, which makes the second integral vanish, and then linearize this equation about ρ^k and $\boldsymbol{v}^k$. The resulting nonlinear partial differential equation is solved by a Newton method based on successive linearization of the PDE. This gives

$$\frac{1}{\Delta t} \int_{\Omega} \delta\rho \ \phi(\boldsymbol{x}) \ d\boldsymbol{x} + \frac{1}{\Delta t} \int_{\Omega} (\rho^k - \rho^{\tau-1})\phi(\boldsymbol{x}) \ d\boldsymbol{x} - \int_{\Omega} (\rho^k v_x^k + v_x^k \delta\rho + \rho^k \delta v_x)\frac{\partial \phi}{\partial x} \ d\boldsymbol{x}$$

$$- \int_{\Omega} (\rho^k v_y^k + v_y^k \delta\rho + \rho^k \delta v_y)\frac{\partial \phi}{\partial y} \ d\boldsymbol{x} = 0,$$

where $\delta\rho = \rho^{k+1} - \rho^k$, $\delta v_x = v_x^{k+1} - v_x^k$, and $\delta v_y = v_y^{k+1} - v_y^k$. For a better readability, we omit the index τ but it is understood to be there. We choose a set of basis functions $\{\phi_i(\boldsymbol{x})\}_{1 \le i \le N}$, where N is the number of mesh nodes for unknowns. Furthermore, we apply the approximation $\delta\rho(\boldsymbol{x}, \tau) \approx \sum_{j=1}^{N} \delta\rho_j(\tau) \ \phi_j(\boldsymbol{x})$, $\delta v_x(\boldsymbol{x}, \tau) \approx \sum_{j=1}^{N} \delta v_{x,j}(\tau) \ \phi_j(\boldsymbol{x})$, and $\delta v_y(\boldsymbol{x}, \tau) \approx \sum_{j=1}^{N} \delta v_{y,j}(\tau) \ \phi_j(\boldsymbol{x})$. Where $\phi_j(\boldsymbol{x})$ are the bilinear basis functions [16]. After substitution in the weak form and

choosing $\phi(\boldsymbol{x}) = \phi_i$, for $i = 1, ..., N$, we obtain

$$\frac{1}{\Delta t} \sum_{j=1}^{N} \delta\rho_j \int_{\Omega} \phi_i(\boldsymbol{x})\phi_j(\boldsymbol{x}) \, d\boldsymbol{x} + \frac{1}{\Delta t} \int_{\Omega} (\rho^k - \rho^{\tau-1})\phi_i(\boldsymbol{x}) \, d\boldsymbol{x}$$

$$- \int_{\Omega} \rho^k v_x^k \frac{\partial \phi_i}{\partial x} d\boldsymbol{x} - \sum_{j=1}^{N} \delta\rho_j \int_{\Omega} v_x^k \phi_j \frac{\partial \phi_i}{\partial x} \, d\boldsymbol{x} - \sum_{j=1}^{N} \delta v_{x,j} \int_{\Omega} \rho^k \phi_j \frac{\partial \phi_i}{\partial x} \, d\boldsymbol{x}$$

$$- \int_{\Omega} \rho^k v_y^k \frac{\partial \phi_i}{\partial y} d\boldsymbol{x} - \sum_{j=1}^{N} \delta\rho_j \int_{\Omega} v_y^k \phi_j \frac{\partial \phi_i}{\partial y} \, d\boldsymbol{x} - \sum_{j=1}^{N} \delta v_{y,j} \int_{\Omega} \rho^k \phi_j \frac{\partial \phi_i}{\partial y} \, d\boldsymbol{x} = 0. \quad (18)$$

The equivalent matrix form of the above equation is given by

$$\frac{1}{\Delta t} M \, \boldsymbol{\delta\rho} + \frac{1}{\Delta t} \boldsymbol{f}_{11} + \boldsymbol{f}_{12} + S_{11} \, \boldsymbol{\delta\rho} + S_{12} \, \boldsymbol{\delta v}_x + S_{13} \, \boldsymbol{\delta v}_y = \boldsymbol{0}.$$

The vector $\boldsymbol{f}_{11}$ and $\boldsymbol{f}_{12}$ are given by

$$\boldsymbol{f}_{11} = M \left(\boldsymbol{\rho}^k - \boldsymbol{\rho}^{\tau-1} \right),$$
$$\boldsymbol{f}_{12} = S_{11} \boldsymbol{\rho}^k.$$

The matrix equation is simplified further by the following substitutions

$$S_\rho = M + \Delta t \, S_{11},$$
$$\boldsymbol{f}_\rho = \boldsymbol{f}_{11} + \Delta t \, \boldsymbol{f}_{12}.$$

Hence the equivalent matrix equation can be written as

$$S_\rho \, \boldsymbol{\delta\rho} + \Delta t \, S_{12} \, \boldsymbol{\delta v}_x + \Delta t \, S_{13} \, \boldsymbol{\delta v}_y + \boldsymbol{f}_\rho = \boldsymbol{0}. \quad (19)$$

By using equation (18), we determine the element mass matrix for the κth element e_κ, $\kappa = 1, 2, .., N_e$ (N_e = number of elements)

$$M_e^{ij} = \delta_{ij} \frac{A_\kappa}{4} \ , \ i, j = 1, 2, 3, 4, \quad (20)$$

where δ_{ij} represents the Kronecker delta and A_κ is the area of the κth element. In this report, we use the following Newton-Cotes quadrature rule (for a rectangle)

$$\int_{e_k} I(x, y) dx dy \approx \frac{1}{4} \sum_{i=1}^{4} I(x_i, y_i). \quad (21)$$

where $\{(x_i, y_i), \ i = 1, 2, 3, 4\}$ are the vertices of an individual element e_κ. Other element matrices and vectors for global matrices and vectors are determined as follows

$$S_{11e}^{ij} = - \int_{e_{xy}} v_x^k \phi_j \frac{\partial \phi_i}{\partial x} \, d\boldsymbol{x} - \int_{e_\kappa} v_y^k \phi_j \frac{\partial \phi_i}{\partial y} \, d\boldsymbol{x}$$

$$= - \frac{A_\kappa}{4} \left(v_{x,j}^k \frac{\partial \phi_i}{\partial x_j} + v_{y,j}^k \frac{\partial \phi_i}{\partial y_j} \right), \quad \text{where } \frac{\partial \phi_i}{\partial x_j} = \frac{\partial \phi_j}{\partial x}|_{x=x_j},$$

$$S_{12e}^{ij} = - \int_{e_\kappa} \rho^k \phi_j \frac{\partial \phi_i}{\partial x} \, d\boldsymbol{x} = - \frac{A_\kappa}{4} \rho_j^k \frac{\partial \phi_i}{\partial x_j},$$

$$S_{13e}^{ij} = - \int_{e_\kappa} \rho^k \phi_j \frac{\partial \phi_i}{\partial y} \, d\boldsymbol{x} = - \frac{A_\kappa}{4} \rho_j^k \frac{\partial \phi_i}{\partial y_j}.$$

For the assembly procedure of global matrices from their corresponding element matrices, we refer to [13]. We also note that an extension of generic convex quadrilateral elements is straightforward by the use of an isoparametric transformation.

3.2. **Integration of the energy equation.** We denote $s = \rho h$ and proceed analogously, as mentioned for the mass equation, in order to obtain the weak formulation for the $2D$ energy equation. We start with the time integration (Euler Backward method),

$$\frac{s^\tau - s^{\tau-1}}{\Delta t} + \boldsymbol{\nabla} \cdot (s^\tau \boldsymbol{v}^\tau) - \boldsymbol{\nabla} \cdot (\lambda \boldsymbol{\nabla} T^\tau) = 0. \tag{22}$$

No heat source is considered, i.e. $q = 0$. The weak form is given by

$$\int_\Omega \frac{s^\tau - s^{\tau-1}}{\Delta t} \phi d\boldsymbol{x} + \int_\Omega \boldsymbol{\nabla} \cdot (s^\tau \boldsymbol{v}^\tau) \phi d\boldsymbol{x} - \int_\Omega \boldsymbol{\nabla} \cdot (\lambda \boldsymbol{\nabla} T^\tau) \phi d\boldsymbol{x} = 0. \tag{23}$$

By substituting

$$\int_\Omega \boldsymbol{\nabla} \cdot (s\boldsymbol{v}) \phi d\boldsymbol{x} = -\int_\Gamma s\phi \boldsymbol{v} \cdot \boldsymbol{n} d\Gamma + \int_\Omega s\boldsymbol{v} \cdot \boldsymbol{\nabla} \phi d\boldsymbol{x}, \tag{24}$$

and using

$$\int_\Omega \boldsymbol{\nabla} \cdot (\lambda \boldsymbol{\nabla} T) \phi d\boldsymbol{x} = \int_\Gamma \lambda \frac{\partial T}{\partial n} \phi d\Gamma - \int_\Omega \lambda \boldsymbol{\nabla} T \cdot \boldsymbol{\nabla} \phi d\boldsymbol{x}, \tag{25}$$

into equation (23), we get

$$\int_\Omega \frac{s^\tau - s^{\tau-1}}{\Delta t} \phi d\boldsymbol{x} + \int_\Gamma s^\tau \eta \boldsymbol{v}^\tau \cdot \boldsymbol{n} d\Gamma - \int_\Omega s^\tau \boldsymbol{v}^{\tau-1} \cdot \boldsymbol{\nabla} \phi d\boldsymbol{x}$$
$$- \int_\Gamma \lambda \frac{\partial T^\tau}{\partial \boldsymbol{n}} \phi d\Gamma + \int_\Omega \lambda \boldsymbol{\nabla} T^\tau \cdot \boldsymbol{\nabla} \phi d\boldsymbol{x} = 0. \tag{26}$$

We apply boundary conditions which eliminate integrals containing boundary terms.

$$\int_\Omega \frac{s^\tau - s^{\tau-1}}{\Delta t} \phi d\boldsymbol{x} - \int_\Omega s^\tau v_x^\tau \frac{\partial \phi}{\partial x} d\boldsymbol{x} - \int_\Omega s^\tau v_y^\tau \frac{\partial \phi}{\partial y} d\boldsymbol{x} + \lambda \int_\Omega \left(\frac{\partial T}{\partial x} \frac{\partial \phi}{\partial x} + \frac{\partial T}{\partial y} \frac{\partial \phi}{\partial y} \right) d\boldsymbol{x} = 0.$$

We linearize these terms about s^k, T^k, v_x^k and v_y^k to get

$$\frac{1}{\Delta t} \int_\Omega \delta s \ \phi(\boldsymbol{x}) \ d\boldsymbol{x} + \frac{1}{\Delta t} \int_\Omega (s^k - s^{\tau-1})\phi(\boldsymbol{x}) \ d\boldsymbol{x} - \int_\Omega (s^k v_x^k + v_x^k \delta s + s^k \delta v_x) \frac{\partial \phi}{\partial x} \ d\boldsymbol{x}$$

$$- \int_\Omega (s^k v_y^k + v_y^k \delta s + s^k \delta v_y) \frac{\partial \phi}{\partial y} \ d\boldsymbol{x} + \lambda \int_\Omega \left[\frac{\partial}{\partial x} \left(\delta T + T^k \right) \frac{\partial \phi}{\partial x} + \frac{\partial}{\partial y} \left(\delta T + T^k \right) \frac{\partial \phi}{\partial y} \right] d\boldsymbol{x} = 0,$$

where δv_x and δv_y were defined previously whereas $\delta s = s^{k+1} - s^k$ and $\delta T = T^{k+1} - T^k$. We apply the approximation $\delta s(\boldsymbol{x}, \tau) \approx \sum_{j=1}^N \delta s_j(\tau)\phi_j(\boldsymbol{x})$ and $\delta T(\boldsymbol{x}, \tau) \approx \sum_{j=1}^N \delta T_j(\tau)\phi_j(\boldsymbol{x})$ to the weak form and hence we obtain

$$\frac{1}{\Delta t} \sum_{j=1}^N \delta s_j \int_\Omega \phi_i \phi_j \ d\boldsymbol{x} + \frac{1}{\Delta t} \int_\Omega (s^k - s^{\tau-1})\phi_i \ d\boldsymbol{x}$$

$$- \int_\Omega s^k v_x^k \frac{\partial \phi_i}{\partial x} d\boldsymbol{x} - \sum_{j=1}^N \delta s_j \int_\Omega v_x^k \phi_j \frac{\partial \phi_i}{\partial x} \ d\boldsymbol{x} - \sum_{j=1}^N \delta v_{x,j} \int_\Omega s^k \phi_j \frac{\partial \phi_i}{\partial x} \ d\boldsymbol{x}$$

$$- \int_\Omega s^k v_y^k \frac{\partial \phi_i}{\partial y} d\boldsymbol{x} - \sum_{j=1}^N \delta s_j \int_\Omega v_y^k s_j \frac{\partial \phi_i}{\partial y} \ d\boldsymbol{x} - \sum_{j=1}^N \delta v_{y,j} \int_\Omega s^k \phi_j \frac{\partial \phi_i}{\partial y} \ d\boldsymbol{x}$$

$$+ \lambda \sum_{j=1}^N \delta T_j \int_\Omega \left(\frac{\partial \phi_i}{\partial x} \frac{\partial \phi_j}{\partial x} + \frac{\partial \phi_i}{\partial y} \frac{\partial \phi_j}{\partial y} \right) d\boldsymbol{x} + \lambda \int_\Omega \left(\frac{\partial T^k}{\partial x} \frac{\partial \phi_i}{\partial x} + \frac{\partial T^k}{\partial y} \frac{\partial \phi_i}{\partial y} \right) d\boldsymbol{x} = 0.$$

The equivalent matrix form of the above equation is given by

$$\frac{1}{\Delta t} M \ \boldsymbol{\delta s} + \frac{1}{\Delta t} \boldsymbol{f}_{21} + \boldsymbol{f}_{22} + S_{11} \ \boldsymbol{\delta s} + S_{22} \ \boldsymbol{\delta v}_x + S_{23} \ \boldsymbol{\delta v}_y + \boldsymbol{f}_{22} + + S_{22} \ \boldsymbol{\delta v}_x + S_{24} \boldsymbol{\delta T} + \boldsymbol{f}_{23} = \boldsymbol{0}.$$

Note that M and S_{11} have already been computed. For the κth element e_κ, the element matrices and vectors for other global matrices and vectors are determined in the following way

$$S_{22e}^{ij} = -\int_{e_\kappa} s^k \phi_j \frac{\partial \phi_i}{\partial x} \, d\boldsymbol{x} = -\frac{A_\kappa}{4} s_j^k \frac{\partial \phi_i}{\partial x_j},$$

$$S_{23e}^{ij} = -\int_{e_\kappa} s^k \phi_j \frac{\partial \phi_i}{\partial y} \, d\boldsymbol{x} = -\frac{A_\kappa}{4} s_j^k \frac{\partial \phi_i}{\partial y_j},$$

$$S_{24e}^{ij} = \lambda \int_{e_\kappa} \left(\frac{\partial \phi_i}{\partial x} \frac{\partial \phi_j}{\partial x} + \frac{\partial \phi_i}{\partial y} \frac{\partial \phi_j}{\partial y} \right) d\boldsymbol{x}$$

$$= \lambda \frac{A_\kappa}{4} \sum_{l=1}^{4} \left(\frac{\partial \phi_i}{\partial x_l} \frac{\partial \phi_j}{\partial x_l} + \frac{\partial \phi_i}{\partial y_l} \frac{\partial \phi_j}{\partial y_l} \right).$$

Again, we make further substitutions to simplify the matrix form of the energy equations, i.e.,

$$\boldsymbol{f}_{22} = S_{11} \boldsymbol{s}^k,$$
$$\boldsymbol{f}_{23} = S_{24} \boldsymbol{T}^k,$$
$$S_s = M + \Delta t \ S_{11},$$
$$\boldsymbol{f}_s = \boldsymbol{f}_{21} + \Delta t \ \boldsymbol{f}_{22} + \Delta t \ \boldsymbol{f}_{23}.$$

Hence the equivalent matrix equation can be written as

$$S_s \ \boldsymbol{\delta s} + \Delta t \ S_{22} \ \boldsymbol{\delta v_x} + \Delta t \ S_{23} \ \boldsymbol{\delta v_y} + \boldsymbol{f}_s + \Delta t \ S_{24} \ \boldsymbol{\delta T} = \boldsymbol{0}. \tag{27}$$

3.3. **Dealing with Darcy's Law.** The horizontal component of Darcy's Law is given by

$$v_x + \frac{K}{\mu} \frac{\partial P}{\partial x} = 0.$$

At time step τ, the weak formulation is given by

$$\int_\Omega v_x^\tau \phi d\boldsymbol{x} + \frac{K}{\mu} \int_\Omega \frac{\partial P^\tau}{\partial x} \phi d\boldsymbol{x} = 0.$$

The linearization of this equation gives

$$\int_\Omega \left(\delta v_x + v_x^k \right) \phi d\boldsymbol{x} + \frac{K}{\mu} \int_\Omega \frac{\partial}{\partial x} (\delta P + P^k) \phi d\boldsymbol{x} = 0.$$

The spatial discretization applied to the above equation yields

$$\sum_{j=1}^{N} \delta v_{x,j} \int_\Omega \phi_i \phi_j d\boldsymbol{x} + \int_\Omega v_x^k \phi_i d\boldsymbol{x}$$

$$+ \frac{K}{\mu} \sum_{j=1}^{N} \delta P_j \int_\Omega \frac{\partial \phi_j}{\partial x} \phi_i d\boldsymbol{x} + \frac{K}{\mu} \int_\Omega \frac{\partial P^k}{\partial x} \phi_i d\boldsymbol{x} = 0,$$

with the following matrix form

$$M \boldsymbol{\delta v_x} + M \boldsymbol{v}_x^k + S_{31} \ \boldsymbol{\delta P} + \boldsymbol{f}_{31} = \boldsymbol{0}.$$

Hence the element matrix and vector are given by

$$S_{31e}^{ij} = \frac{K}{\mu} \int_{e_\kappa} \frac{\partial \phi_j}{\partial x} \phi_i d\boldsymbol{x} = A_\kappa \frac{K}{4\mu} \frac{\partial \phi_j}{\partial x_i}.$$

$$\boldsymbol{f}_{31} = S_{31} \boldsymbol{P}^k.$$

For a later use we define

$$\boldsymbol{f}_x = \boldsymbol{f}_{31} + M \boldsymbol{v}_x^k.$$

The treatment of the vertical component of Darcy's Law is analogous, and gives the matrix form

$$M\boldsymbol{\delta v_y} + M\boldsymbol{v}_y^k + S_{41}\ \boldsymbol{\delta P} + \boldsymbol{f}_{41} = \boldsymbol{0},$$

where

$$S_{41_e}^{ij} = A_\kappa \frac{K}{4\mu} \frac{\partial \phi_j}{\partial y_i}.$$

$$f_{41_e}^i = S_{41}\boldsymbol{P}^k,$$

and

$$\boldsymbol{f}_y = \boldsymbol{f}_{41} + M\boldsymbol{v}_y^k.$$

3.4. **Thermodynamical relations for the temperature and pressure.** We obtain the temperature (and pressure) vector by using the density and enthalpy values through available phase diagrams, i.e.,

$$T = T(\rho, h).$$

In this case, linearization results into

$$T^k - T(\rho^k, h^k) + \delta T - \frac{\partial T}{\partial \rho}\delta\rho - \frac{\partial T}{\partial h}\delta h = 0,$$

where $\frac{\partial T}{\partial \rho}$ is approximated by

$$\frac{\partial T}{\partial \rho} \approx \frac{T(\rho^k + \epsilon, h^k) - T(\rho^k, h^k)}{\epsilon}.$$

Here ϵ is a suitable small number (we use $\epsilon = .001$). The approximation for $\frac{\partial T}{\partial h}$ is analogous. Now, the spatial discretization takes the following form

$$I\ \boldsymbol{\delta T} + S_{51}\ \boldsymbol{\delta\rho} + S_{52}\ \boldsymbol{\delta h} + \boldsymbol{f}_T = \boldsymbol{0}. \tag{28}$$

Here I is an identity matrix whereas S_{51} and S_{52} are diagonal matrices

$$S_{51}^{ij} = -\frac{\partial T}{\partial \rho} = -\frac{T(\rho_i^k + \epsilon, h_i^k) - T(\rho_i^k, h_i^k)}{\epsilon}\delta_{ij},$$

$$S_{52}^{ij} = -\frac{\partial T}{\partial h} = -\frac{T(\rho_i^k, h_i^k + \epsilon) - T(\rho_i^k, h_i^k)}{\epsilon}\delta_{ij},$$

$$f_T^i = T_i^k - T(\rho_i^k, h_i^k),$$

where δ_{ij} represents the Kronecker Delta. For the pressure variable we have,

$$P = P(\rho, h).$$

The linearization procedure is similar to the temperature case, i.e.,

$$P^k - P(\rho^k, h^k) + \delta P - \frac{\partial P}{\partial \rho}\delta\rho - \frac{\partial P}{\partial h}\delta h = 0,$$

The matrix form is

$$I\ \boldsymbol{\delta P} + S_{61}\ \boldsymbol{\delta\rho} + S_{62}\ \boldsymbol{\delta h} + \boldsymbol{f}_P = \boldsymbol{0}. \tag{29}$$

Again, S_{61} and S_{62} are diagonal matrices

$$S_{61}^{ij} = -\frac{\partial P}{\partial \rho} = -\frac{P(\rho_i^k + \epsilon, h_i^k) - P(\rho_i^k, h_i^k)}{\epsilon}\delta_{ij},$$

$$S_{62}^{ij} = -\frac{\partial P}{\partial h} = -\frac{P(\rho_i^k, h_i^k + \epsilon) - P(\rho_i^k, h_i^k)}{\epsilon}\delta_{ij},$$

$$f_P^i = P_i^k - P(\rho_i^k, h_i^k).$$

3.5. The density, enthalpy and total enthalpy relation.

The relation between the density, enthalpy, and total enthalpy is given by

$$s = \rho h. \tag{30}$$

Linearization of this equation is given as

$$s^k - \rho^k h^k + \delta s - \rho^k \delta h - h^k \delta \rho = 0. \tag{31}$$

The matrix form is

$$I \, \boldsymbol{\delta s} + S_{71} \, \boldsymbol{\delta \rho} + S_{72} \, \boldsymbol{\delta h} + \boldsymbol{f}_h = \boldsymbol{0}, \tag{32}$$

where

$$S_{71}^{ij} = -h_i^k \delta_{ij},$$
$$S_{72}^{ij} = -\rho_i^k \delta_{ij},$$
$$f_h^i = s_i^k - \rho_i^k h_i^k.$$

To summarize, we solve the following set of equations

$$
\begin{aligned}
S_\rho \, \boldsymbol{\delta\rho} + \Delta t \, S_{12} \, \boldsymbol{\delta v}_x + \Delta t \, S_{13} \, \boldsymbol{\delta v}_y + \boldsymbol{f}_\rho = \boldsymbol{0}, && \text{(mass equation)}, \\
S_s \, \boldsymbol{\delta s} + \Delta t \, S_{22} \, \boldsymbol{\delta v}_x + S_{23} \, \boldsymbol{\delta v}_y + \Delta t \, S_{24} \, \boldsymbol{\delta T} + \boldsymbol{f}_s = \boldsymbol{0}, && \text{(energy equation)}, \\
M \, \boldsymbol{\delta v} + S_{31} \, \delta P + \boldsymbol{f}_x = \boldsymbol{0}, && \text{(Darcy's law, x-axis)}, \\
M \, \boldsymbol{\delta v} + S_{41} \, \delta P + \boldsymbol{f}_y = \boldsymbol{0}, && \text{(Darcy's law, y-axis)}, \\
I \, \boldsymbol{\delta T} + S_{51} \, \boldsymbol{\delta\rho} + S_{52} \, \boldsymbol{\delta h} + \boldsymbol{f}_T = \boldsymbol{0}, && (T = T(\rho, h)), \\
I \, \boldsymbol{\delta P} + S_{61} \, \boldsymbol{\delta\rho} + S_{62} \, \boldsymbol{\delta h} + \boldsymbol{f}_P = \boldsymbol{0}, && (P = P(\rho, h)), \\
I \, \boldsymbol{\delta s} + S_{71} \, \boldsymbol{\delta\rho} + S_{72} \, \boldsymbol{\delta h} + \boldsymbol{f}_h = \boldsymbol{0}, && (s = \rho h).
\end{aligned}
$$

For a Newton Raphson loop, the Jacobian is expressed in the following block matrix form

$$
J = \begin{bmatrix}
S_\rho & \mathbf{0} & \Delta t \, S_{12} & \Delta t \, S_{13} & \mathbf{0} & \mathbf{0} & \mathbf{0} \\
\mathbf{0} & S_s & \Delta t \, S_{22} & \Delta t \, S_{23} & \Delta t \, S_{24} & \mathbf{0} & \mathbf{0} \\
\mathbf{0} & \mathbf{0} & M & \mathbf{0} & \mathbf{0} & S_{31} & \mathbf{0} \\
\mathbf{0} & \mathbf{0} & \mathbf{0} & M & \mathbf{0} & S_{41} & \mathbf{0} \\
S_{51} & \mathbf{0} & \mathbf{0} & \mathbf{0} & I & \mathbf{0} & S_{52} \\
S_{61} & \mathbf{0} & \mathbf{0} & \mathbf{0} & \mathbf{0} & I & S_{62} \\
S_{71} & I & \mathbf{0} & \mathbf{0} & \mathbf{0} & \mathbf{0} & S_{72}
\end{bmatrix}_{7N \times 7N},
$$

$$
\boldsymbol{F} = \begin{bmatrix}
\boldsymbol{f}_\rho \\
\boldsymbol{f}_s \\
\boldsymbol{f}_x \\
\boldsymbol{f}_y \\
\boldsymbol{f}_T \\
\boldsymbol{f}_P \\
\boldsymbol{f}_h
\end{bmatrix}_{7N \times 1}, \qquad
\boldsymbol{G}^k = \begin{bmatrix}
\boldsymbol{\rho}^k \\
\boldsymbol{s}^k \\
\boldsymbol{v}_x^k \\
\boldsymbol{v}_y^k \\
\boldsymbol{T}^k \\
\boldsymbol{P}^k \\
\boldsymbol{h}^k
\end{bmatrix}_{7N \times 1}.
$$

Finally, the Newton Raphson loop is given by,

$$\boldsymbol{G}^{k+1} = \boldsymbol{G}^k - J^{-1} \boldsymbol{F}. \tag{33}$$

where J_{-1} is computed by Gaussian elimination.

4. Numerical Experiments

A number of study cases are provided and discussed in this section. We assume no heat source ($q = 0$) for the given examples. It is important to mention that , for our test problems, the method is unconditionally stable for continuous initial values. The value of Δt can be chosen equal to the process time (t_{max}) and hence the system can be solved in one time step (with few Newton-Raphson iterations). So

the reasons to choose a relatively small Δt are only given by accuracy and desire to follow the kinetics of the process. Therefore, we select a suitably small Δt to observe variables profile in the transitional stage. In case of the Picard iteration, used in [2], we needed $\Delta t = 1/(10 \times \Delta x^2) \approx 1/10^5$ which requires 4×10^5 iterations for a process time of 4 seconds. This gave excessive computation times regardless of the applied boundary conditions which made the method not feasible for applications in higher dimensions.

4.1. **Case Study 1. Piecewise linear $1D$ conditions with $1D$ model.** In this case study we use the following conditions

$$T(x,0) = \begin{cases} 290 & \text{for } x \in [0, 0.05], \\ 290 + \frac{10}{9}x - \frac{1}{18} & \text{for } x \in]0.05, 0.95], \\ 291 & \text{for } x \in]0.95, 1], \end{cases}$$

$$\Delta t = 1/10 \ [s] \qquad\qquad \text{(time step)},$$
$$\Delta x = 1/99 \qquad\qquad \text{(spatial step)},$$
$$\epsilon_r = 10^{-6} \qquad\qquad \text{(error tolerance on } \rho \text{ and } h),$$
$$K = 5 \times 10^{-11} \ [m^2],$$
$$\mu = 5 \times 10^{-5} \ [P_a \ s],$$
$$\lambda = 0.05 \ [W/m/K],$$
$$t_{max} = 4.0 \ [s] \qquad\qquad \text{(process time)}.$$

We used homogeneous natural boundary conditions. The solution plots are shown
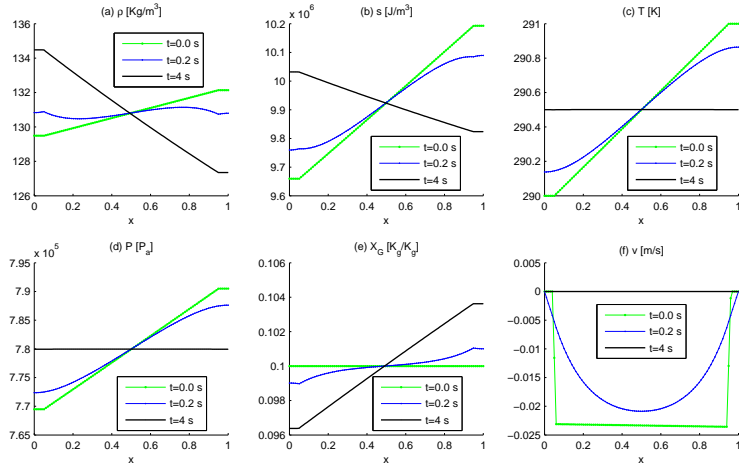
FIGURE 3. Case Study 1. Solution plots of the $1D$ fluid system with piecewise linear initial conditions and $\Delta t = 1/10 \ [s]$, $\Delta x = 1/99 \ [m]$, and $\epsilon_r = 10^{-6}$. The plots are (a) the density, (b) total enthalpy, (c) temperature, (d) pressure, (e) gas mass-fraction, and (f) velocity.

in Figure 3 and we explain their validity in the following paragraphs.

4.1.1. *The temperature and pressure plots.* The initial value of T is a piecewise linear function. Fourier's Law of heat conduction dictates that the heat flows from a higher temperature point to a lower temperature point. Following this law, the steady-state value of T is a constant. Hence the temperature profiles at $t = 0, \ 0.2, \ 4.0 \ [s]$ agree

qualitatively to Fourier's Law although we solve a different nonlinear problem here. The pressure P is a monotonically increasing function of T within our operating conditions (refer to Figure 2). Therefore, the P plots should have a spatial profile similar to T for a small variation in T and this actually is the case.

4.1.2. *The velocity and density plots.* Once we have P values, it is relatively simple to verify v values through Darcy's Law. The plots of v, as given in Figure 3(e) are consistent with the plots given for P. For a negative velocity (right to left) the fluid mass increases in the left part of the domain (for an insulated system). Hence the density increases in the left part and decreases in the right part of the domain.

4.1.3. *The gas mass fraction plots.* At constant temperature, the region with a lower density contains more gas mass fraction as compared to the region where the density has a higher value. With this argument we actually justify the steady-state X_G plot. The X_G plot at $t = 0$ represents the initial condition and the X_G plot at $t = 0.2$ shows an intermediate stage.

4.1.4. *The total enthalpy plots.* The mass and heat energy flows from right to left and therefore the total enthalpy s increases in the left part of the domain until the system attains its steady-state value.

To this point we have justified qualitatively all simulation results given in Figure 3. Furthermore, we checked for mass and energy conservation by computing the total mass ($\int_\Omega \rho d\boldsymbol{x}$) and the total energy ($\int_\Omega s d\boldsymbol{x}$) at each time iteration and found that these quantities are indeed conserved in our numerical solutions.

4.2. **Case Study 2. Piecewise linear $1D$ conditions with $2D$ model.** In this case study we use the following conditions

$$T(\boldsymbol{x}, 0) = \begin{cases} 290 & \text{for } x \in [0, 0.05], \ y \in [0, 1], \\ 290 + \frac{10}{9}x - \frac{1}{18} & \text{for } x \in]0.05, 0.95], \ y \in [0, 1], \\ 291 & \text{for } x \in]0.95, 1], \ y \in [0, 1], \end{cases}$$

$$\Delta t = 1/10,$$
$$\Delta x = 1/99,$$
$$\Delta y = 1/99,$$
$$\epsilon_r = 10^{-6},$$

with homogeneous natural boundaries everywhere on the boundary. These are precisely the same conditions as we use for Case Study 1, except that here we solve a $2D$ model over a unit square. With these conditions the density plots are given in Figure 4(a) to (c). A comparison of the cross-section of density plots is made with the solution obtained from the Case Study 1 and it is given in Figure 4(d) to (f). The relative difference is negligible. The temperature and gas mass fraction plots are shown in Figure 5(a)-(c) and in Figure 5(d)-(f), respectively. The temperature and gas mass fraction plots are also compared with the plots obtained from Case Study 1 (not shown here), the relative difference is again less than 10^{-10}. Furthermore, we apply similar conditions in y-direction i.e.,

$$T(\boldsymbol{x}, 0) = \begin{cases} 290 & \text{for } y \in [0, 0.05], \ x \in [0, 1], \\ 290 + \frac{10}{9}y - \frac{1}{18} & \text{for } y \in]0.05, 0.95], \ x \in [0, 1], \\ 291 & \text{for } y \in]0.95, 1], \ x \in [0, 1], \end{cases}$$

and compared the solution results with the case when conditions are in the x-direction. The relative difference is negligible. All these comparisons, at least, indicate that the solution algorithm is consistent regardless of dimensionality and initial conditions (or flow direction).
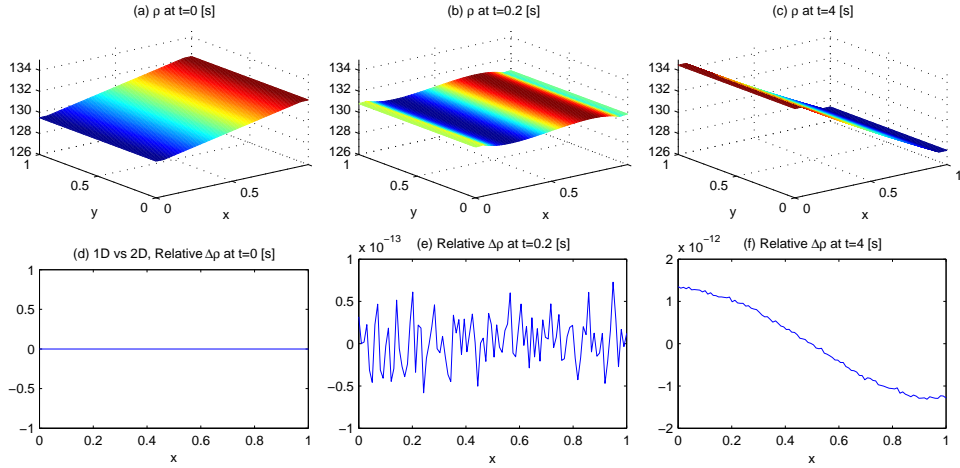
FIGURE 4. Case Study 2. Solution plots of the $2D$ fluid system with piecewise linear initial conditions in T along x-axis, (see initial conditions), with $\Delta t = 1/10$, $\Delta x = 1/99$, and $\epsilon_r = 10^{-6}$. The solution plots are (a) the density (ρ_j), $j = 1, 2, ..., N$, at $t = 0$ $[s]$, (b) ρ_j at $t = 0.2$ $[s]$, (c) ρ_j at $t = 4$ $[s]$, (d) $\frac{\rho_j^{2D} - \rho_j^{1D}}{\rho_j^{1D}}$, at $t = 0$, (e) $\frac{\rho_j^{2D} - \rho_j^{1D}}{\rho_j^{1D}}$ at $t = 0.2$, and (f) $\frac{\rho_j^{2D} - \rho_j^{1D}}{\rho_j^{1D}}$ at $t = 4$ $[s]$.
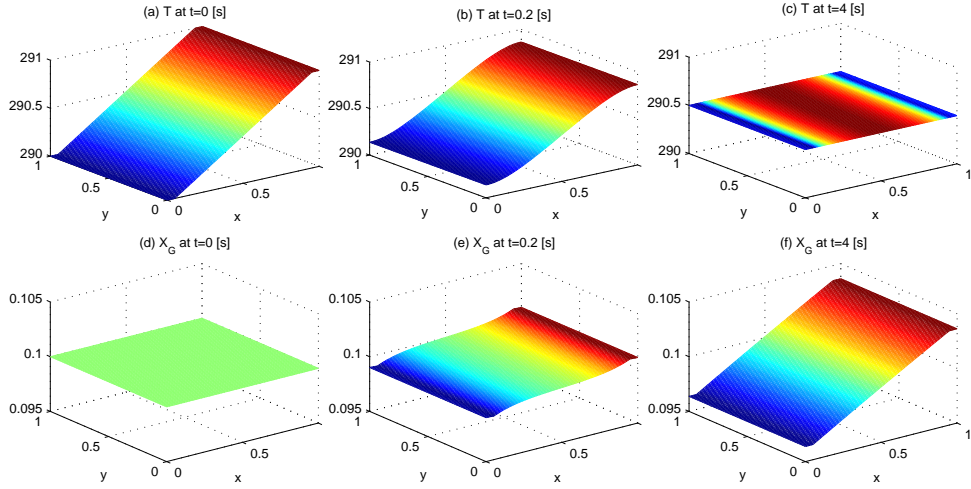
FIGURE 5. Case Study 2. Piecewise linear initial conditions in T along x-axis, with $\Delta t = 1/10$, $\Delta x = 1/99$, and $\epsilon_r = 10^{-6}$. The solution plots are (a) the temperature T at $t = 0$ $[s]$, (b) T at $t = 0.2$ $[s]$, (c) T at $t = 4$ $[s]$, (d) gas mass fraction X_G at $t = 0$, (e) X_G at $t = 0.2$, and (f) X_G at $t = 4$ $[s]$.

4.3. **Case Study 3. The solution of of $2D$ model with $2D$ conditions.** In this case we set the following conditions

$$T(\boldsymbol{x}, 0) = 290 + I_p,$$

$$I_p = \begin{cases} -\frac{20}{9}x + \frac{10}{9} & \text{for } x \in [0.05, 0.5], \ y \in [0.5, 1 - x] \cup [x, 0.5], \\ \frac{20}{9}x - \frac{10}{9} & \text{for } x \in [0.5, 0.95], \ y \in [1 - x, 0.5] \cup [0.5, x], \\ -\frac{20}{9}y + \frac{10}{9} & \text{for } y \in [0.05, 0.5], \ x \in [0.5, 1 - y] \cup [y, 0.5], \\ \frac{20}{9}y - \frac{10}{9} & \text{for } y \in [0.5, 0.95], \ x \in [1 - y, 0.5] \cup [0.5, y], \\ 1 & \text{for other } (x, y) \in \Omega. \end{cases}$$

$$\Delta t = 1/20,$$

$$\Delta x = \Delta y = 1/99,$$

$$K = 5 \times 10^{-11},$$

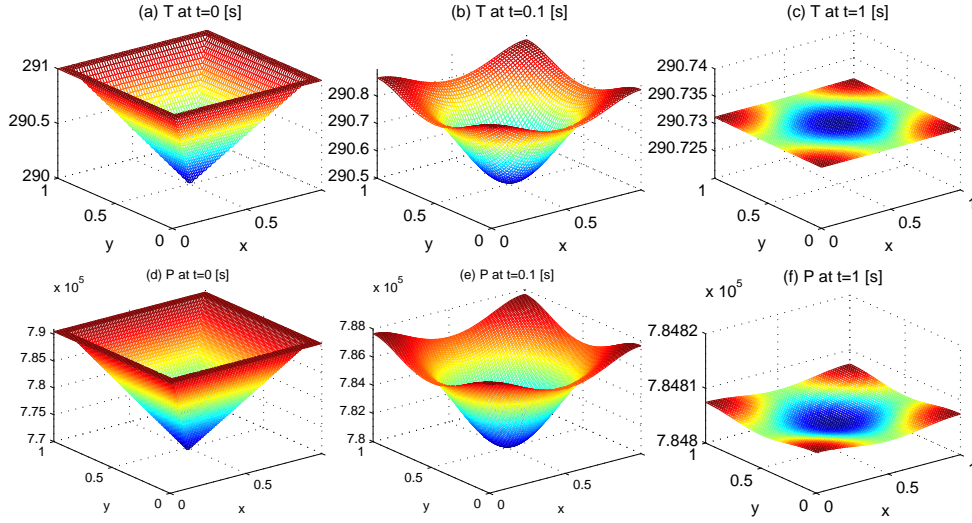with homogeneous natural boundaries everywhere on the boundary. Here I_p is a
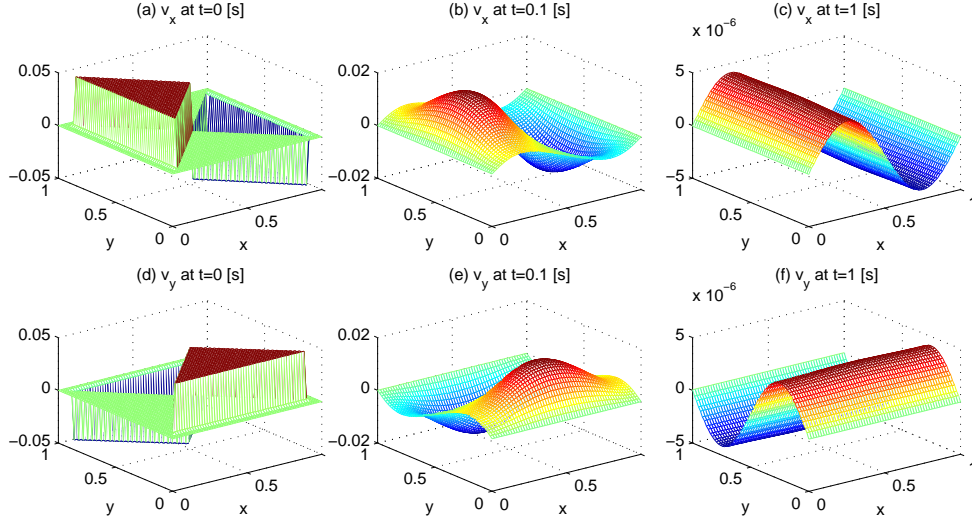

FIGURE 6. Case Study 3. Solution plots for $2D$ model with $2D$ conditions, (a) T at $t = 0$ $[s]$, (b) T at $t = 0.1$ $[s]$, (c) T at $t = 1$ $[s]$, (d) P at $t = 0$ $[s]$, (e) P at $t = 0.1$ $[s]$, and (f) P at $t = 1$ $[s]$.

FIGURE 7. Case Study 3. Solution plots for $2D$ model with $2D$ conditions, (a) v_x at $t = 0$ $[s]$, (b) v_x at $t = 0.1$ $[s]$, (c) v_x at $t = 1$ $[s]$, (d) v_y at $t = 0$, (e) v_y at $t = 0.1$, and (f) v_y at $t = 1$.

squeezed inverted pyramid function with a unit height. The boundary is located at a height $z = 1$ and center point is at ($x = 0.5$, $y = 0.5$, $z = 0$). The pyramid fits within the domain $x \in [0.05, 0.95]$, $y \in [0.05, 0.95]$. The remaining 0.05 wide strip is a constant height function $z = 1$. This ensures an initially zero velocity normal to the boundary. Although this example is solved over a mesh with 100×100 nodes but we give their plots with slightly reduced mesh density (60×60 nodes) for the sake of faster printing. The explanation for the solution variable plots as given for

Case Study 1 applies to these plots as well. For example, the solution variable T evolves to a constant steady-state profile (as shown in Figure 6), P follows a pattern similar to T 6) since $\frac{\partial P}{\partial X_G} = 0$, v follows from P through Darcy's law to show an inward direction from each side (Figure 7), and ρ increases in the central portion of the domain in response to an inward velocity (Figure 8), etc. The X_G is plotted in Figure 10 for the initial, transient, and steady-state values. This example shows that the model and the solution algorithm is robust to handle discontinuous initial conditions (e.g., an initial discontinuous velocity). Next two examples also support this argument.
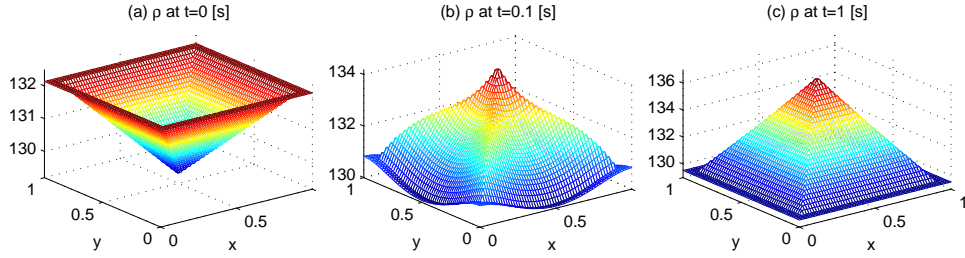
FIGURE 8. Case Study 3. Solution plots for $2D$ model with $2D$ conditions. $\Delta t = 1/20$, $\Delta x = \Delta y = 1/99$, $\epsilon_r = 10^{-6}$. The plots are (a) ρ at $t = 0$ $[s]$, (b) ρ at $t = 0.1$ $[s]$, and (c) ρ at $t = 1$ $[s]$.
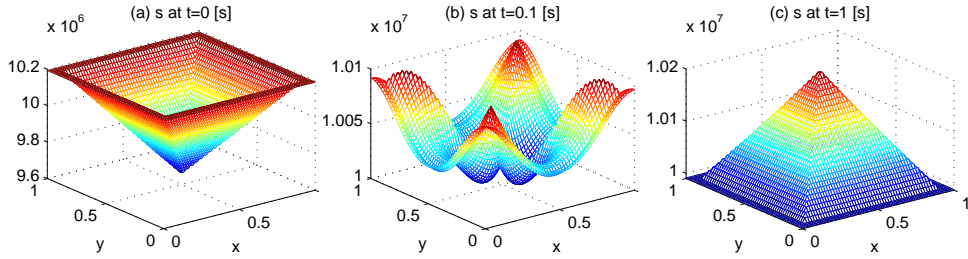

FIGURE 9. Case Study 3. Solution plots for $2D$ model with $2D$ conditions, (a) s at $t = 0$ $[s]$, (b) s at $t = 0.1$ $[s]$, and (c) s at $t = 1$ $[s]$.
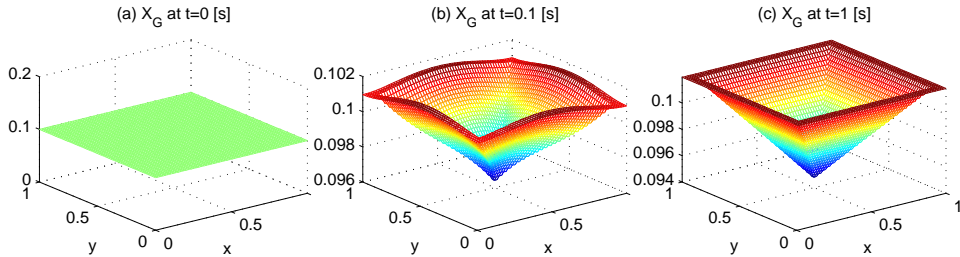

FIGURE 10. Case Study 3. Solution plots for $2D$ model with $2D$ conditions, (a) X_G at $t = 0$ $[s]$, (b) X_G at $t = 0.1$ $[s]$, and (c) X_G at $t = 1$ $[s]$.

17

4.4. **Case Study 4. Tracking of a sharp phase interface.** In this $1D$ example, we set X_G initially equal to a step function and T is set piecewise linear so that we obtain a nonzero velocity for the phase interface. Let $\Gamma(t)$ be a function which represents the position of the phase front at time t i.e.,

$$\Gamma(t) := \left\{ x \in \Omega, t \geq 0 | X_G(x,t) = \hat{X_G} \right\}$$

We use the following initial conditions.

$$X_G(x,0) = \begin{cases} 0.1 & \text{for } x \in [0, 0.5], \\ 0.2 & \text{for } x \in]0.5, 1], \end{cases}$$

$$T(x,0) = \begin{cases} 285 & \text{for } x \in [0, 0.05], \\ 285 + \frac{200}{9}x - \frac{20}{18} & \text{for } x \in]0.05, 0.95], \\ 305 & \text{for } x \in]0.95, 1]. \end{cases}$$

For this example, $\Delta x = 1/999$ and $\Delta t = 1/50$ is used. For a discontinuous initial X_G, the problem can not be solved in one time step but $\Delta t = 1/50$ $[s]$ is still a large number as compared to the value of Δt used for Picard iteration and the IMEX method. After a few time iterations (e.g., 3), the X_G profile becomes smooth and Δt can be adapted to a larger value. In Figure 11, we provide, (a) the initial value for T, (b) the initial and steady-state values for X_G, and (c) a comparison between $\Gamma(t)$ and $g(t) = \alpha + \beta\sqrt{t}$ for empirically chosen $\alpha = 0.5515$ and $\beta = -0.37$. The phase tracking as part of the solution in moving boundary problems, such as
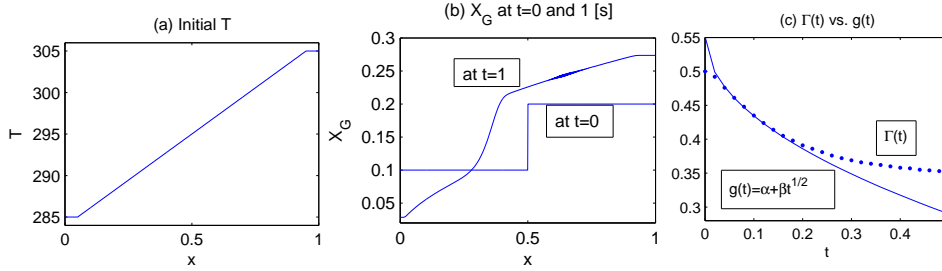

FIGURE 11. Case Study 4. Solution plots for (a) the initial T, (b) the initial and steady-state X_G, and (c) a comparison between $\Gamma(x,t)$ and $g(t) = \alpha - \beta\sqrt{t}$ with $\alpha = 0.5515$ and $\beta = 0.37$.

Stefan problem, gives a function of the form $g(t) = \alpha + \beta\sqrt{t}$. Since we consider an insulated system, with no heat source in it, it attains a steady-state asymptotically. This means that there is a Γ^∞ such that $\Gamma(t) \to \Gamma^\infty$ as $t \to \infty$. Hence, we do not expect $\Gamma(t)$ to follow $g(t)$ for a longer time interval. The function $\Gamma(t)$ however approximately matches with $g(t)$ at early stages only. Although, near $t = 0$ (at the very early stage), there seems to be a different behavior. This deviation is acceptable at the first iteration because some of the variables are discontinuous at $t = 0$. Hence, even the first weak derivative of ρ, for instance, does not exist. Therefore the approximation made from the Taylor series in Section 2.3, which was used to derive the Newton method, can not give an accurate solution at $t = 0$. This fact is shown in Figure 11(c). We conclude that the ρ-h model can be used to solve sharp interface problems with diffusion-like mechanisms.

4.5. **Case Study 5. Semicircular phase front.** In this example, we use $\Delta x = 1/199$, $\Delta y = 1/199$, $\Delta t = 1/50$, and the process time $t_{max} = 1.0$ $[s]$ and set the

following initial conditions

$$X_G(\boldsymbol{x},0) = \begin{cases} 0.1 & \text{for } x^2 + y^2 \le 0.5, \ x, y \ge 0, \\ 0.2 & \text{for } x^2 + y^2 > 0.5, \ 0 \le x, y \le 1, \end{cases}$$

$$T(\boldsymbol{x},0) = \frac{1}{2}(T_1 + T_2),$$

$$T_1 = \begin{cases} 305 & \text{for } x \in [0, 0.05], \ y \in [0, 1], \\ 305 - \frac{200}{9}x + \frac{20}{18} & \text{for } x \in]0.05, 0.95], \ y \in [0, 1], \\ 285 & \text{for } x \in]0.95, 1], \ y \in [0, 1], . \end{cases}$$

$$T_2 = \begin{cases} 305 & \text{for } y \in [0, 0.05], \ x \in [0, 1], \\ 305 - \frac{200}{9}y + \frac{20}{18} & \text{for } y \in]0.05, 0.95], \ x \in [0, 1], \\ 285 & \text{for } y \in]0.95, 1], \ x \in [0, 1], \end{cases}$$

By setting T in this way, we ensure a $2D$ initial flow in general but a zero normal velocity at every boundary point. Figure 12 shows the initial values of T and X_G whereas the contour plot in Figure 13 contains the initial and steady-state position of the phase front. It can be seen that the displacement of the edge is most pronounced along the line $y = x$. This is a consequence of the fact that the distance to the boundaries is maximal at $y = x$, by which the fluids can be transported more rapidly by the nonlinear (cross) diffusion mechanism. In this example we show that the model works well for $2D$ conditions for the tracking of sharp interfaces.
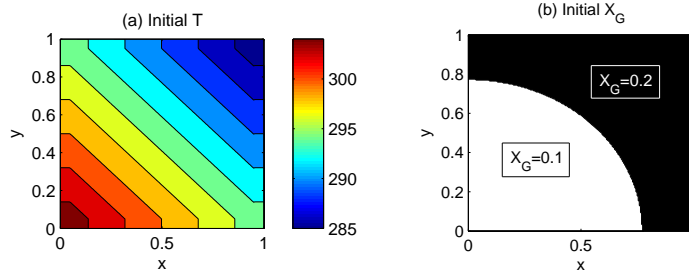

FIGURE 12. Case Study 5. Solution plots for (a) T at $t = 0$ $[s]$ and (b) X_G at $t = 0$.
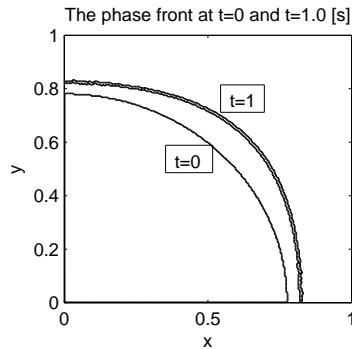

FIGURE 13. Case Study 5. The initial and steady-state value of the phase front.

5. Conclusions and further work

We developed a successful strategy to solve the PDE's in the (ρ, h)-formulation of multi-phase flow. To wrap up, the most important conclusions are

- Newton-Raphson linearization together with the standard Galerkin algorithm enables to choose a large Δt with respect to stability and to solve the system efficiently.
- Picard iteration combined with the initial guess equal to the solution variables from the previous time step leads to excessively small time-step Δt. The same is concluded for the IMEX time integration method.
- Certain thermodynamical relations, such as $\frac{\partial P}{\partial X_G} = 0$, between solution variables make the problem, with nonhomogeneous Robin boundary conditions, ill-posed.
- For a problem where the initial X_G is discontinuous, the selection of a time-step for a stable solution is affected by the choice of certain parameters (e.g., K) and also by the initial temperature gradient. We found that an adaptive time-step will enable us for choosing eventually larger time-steps, for discontinuous problems.

The model, which currently consists of seven equations to be solved by Newton-Raphson method, can be reduced to a two equation system. It is expected that the two equation system will enable an analytic treatment of this system with respect to convergence behavior, to analyze the numerical methods in more mathematical rigor, and to analyze the model equations qualitatively. This will be done in future studies.

References

[1] A. R. J. Arendsen, A. I. van Berkel, A. B. M. Heesink, and G. F. Versteeg. Dynamic modelling of thermal processes with phase transitions by means of a density-enthalpy phase diagram. 7th World Congress of Chemical Engineering, Glasgow, Scotland, 2005.

[2] Ibrahim, F. J. Vermolen, and C. Vuik. Application of the numerical density-enthalpy method to the multi-phase flow through a porous medium. Procedia Computer S, cience 1 (2010) 781-790, Amsterdam, The Netherlands, 2010.

[3] A. R. J. Arendsen and G. F. Versteeg. Dynamic modelling of refrigeration cycles using density and enthalpy as state variables. 17th International Congress of Chemical and Process Engineering, Prague, The Czech Republic, 2006.

[4] A. R. J. Arendsen and G. F. Versteeg. Dynamic Thermodynamics with Internal Energy, Volume, and Amount of Moles as States: Application to Liquefied Gas Tank. Ind. Eng. Chem. Res. 2009, 48, 3167-3176.

[5] M. Fabbri and V. R. Voller. The Phase-Field Method in the Sharp-Interface Limit: A comparison between Model Potentials. Journal of Computational Physics, 1997.

[6] A. Abouhafç. Finite Element Modeling Of Thermal Processes With Phase Transitions. Master Thesis, 2007, Delft University of Technology.

[7] Ibrahim, C. Vuik, F.J. Vermolen, D. Hegen. Numerical Methods for Industrial Flow Problems. Delft University of Technology, Report 08-13, 2008.

[8] E. Javierre, C. Vuik, F. J. Vermolen, S. van der Zwaag. A comparison of numerical models for one-dimensional Stefan problems. J. Comp. Appl. Math., 2006, 192, 445-459.

[9] H. Emmerich. The Diffuse Interface Approach in Materials Science, Thermodynamic Concepts and Applications of Phase-Field Models. Springer, Berlin, 2003.

[10] J.H. Brusche, A. Segal, and C. Vuik. An efficient numerical method for solid-liquid transitions in optical rewritable recording. International Journal for Numerical Methods in Engineering, 77, pp. 702-718, 2009.

[11] O.C. Zienkiewicz, R.L. Taylor, & J.Z. Zhu. The Finite Element Method, Its Basis & Fundamentals. 6e, Butterworth-Heinemann, 2005.

[12] K. A. Hoffmann. Computational Fluid Dynamics, Vol I. 4e, EES, Wichita, USA, 2000.

[13] J. van Kan, A Segal, F. Vermolen. Numerical Methods in Scientific Computing. VSSD, 2004.

[14] R. J. Leveque. Finite Volume Methods for Hyperbolic Problems. Cambridge University Press, USA, 2002.

[15] J.N. Reddy. An Introduction to the Finite Element Method. 2e, McGraw-Hill, 1993.

[16] Ibrahim, C. Vuik, F.J. Vermolen, D. Hegen. Numerical Methods for Industrial Flow Problems. Delft University of Technology, Report 09-10, 2009.

[17] H. S. Udaykumar, R. Mittal, and W. Shyy. Computation of SolidLiquid Phase Fronts in the Sharp Interface Limit on Fixed Grids. Journal of Computational Physics 153, 1999, 535-574.

[18] S. Chen , B. Merriman , S. Osher , P. Smereka. A simple level set method for solving Stefan problems. Journal of Computational Physics, v.135 n.1, p.8-29, July 15, 1997.

[19] S. Osher , J. A. Sethian. Fronts propagating with curvature-dependent speed: algorithms based on Hamilton-Jacobi formulations. Journal of Computational Physics, v.79, pp.12-49, Nov. 1988.

[20] A. Faghri, Y. Zhang, J. Howell. Advanced Heat and Mass Transfer. Global Digital Press, 2010.

[21] B. Nedjar. An enthalpy-based finite element method for nonlinear heat problems involving phase change. Comput. Struct. 80 (2002) 9-21.

[22] G. Comini, S. DelGiudice, B. W. Lewis, O. C. Zienkiewicz. Finite element solution of nonlinear heat conduction problems with special reference to phase change. Int. J. Numer. Meth. Engng., 8, pp. 613624, 1974.

[23] G. Segal, C. Vuik and F. J. Vermolen. A conserving discretization for the free boundary in a two-dimensional Stefan problem. J. Comp. Phys., 141, pp. 1-21, 1998.